Spring 5-1-2013

Research and Development of the Positron Damping Rings for the Proposed International Linear Collider and at CERN in Geneva, Switzerland for the Large Hadron Collider ATLAS Experiment's Integrated Simulation Framwork

Ryan Badman
Syracuse University

Comparing ECLOUD Simulation Results to 2.1 and 5.3 GeV Positron Shielded Pickup Data

Ryan P. Badman
Department of Physics, Syracuse University, Syracuse, NY, 13210
(Dated: August 12, 2011)

The CesrTA group researches the mitigation of the electron cloud in the Cornell synchrotron beam pipe by taking measurements of the cloud density and cloud effects on the beam. Various simulation programs are then used to try to study the physics behind cloud formation and beam quality at different cloud densities. The results presented here are from the ECLOUD program and concentrate on matching data from witness bunch scans that studied the relative cloud density at different bunch spacings to measure cloud decay over time. After many simulations runs, parameters were found for both 2.1 and 5.3 GeV at 5 mA per bunch that successfully caused agreement between simulation and data and the values for these parameters will be given below. Upper and lower bounds were also found for the SEMAX parameter in the secondary energy distribution, and the secondary energy distribution was optimized to cause better agreement between peak shapes in the simulation and data.

I. INTRODUCTION

Electron clouds are an important phenomenon to study in circular particle accelerators such as the LHC, the Cornell synchrotron, and the damping ring for the ILC. Low energy background electrons are normally present in high energy accelerators and are often not detrimental to beam performance, but certain operation conditions cause them to interact strongly with the beam, as was first observed in the 1980s in positron storage rings [1]. The generation and amplification of the electron cloud is caused by ionization of residual gas in the vacuum chamber and irradiation of the chamber wall by synchrotron radiation [1]. Multipacting is when electrons are accelerated by the electric field created by the beam to a high enough energy that they produce more than one secondary electron per collision with the vacuum chamber wall on average, leading to a large cloud buildup [2]. These clouds can have many detrimental effects on the beam performance, including beam degradation and tune shift. Electron clouds have also caused the degradation of BPM signals and feedback pick-ups, a problem that can be partially solved by higher frequency data processing or the use of solenoids [3]. Proton and positron beams are more vulnerable to cloud effects than electron beams because of Coulomb attraction due to opposite charge. The cloud can be mitigated by changing vacuum chamber surface roughness such as by adding a sawtooth pattern on the chamber wall, coating the chamber with materials such as titanium nitride as used in this study, or by applying a solenoidal field [4]. A 1 micron thick coating of TiN is enough to reduce multipacting in the vacuum chamber because of the material's low secondary yield, and a solenoidal field of about 50 G keeps electrons near the wall to avoid interactions with the beam [2].

Primary electrons are produced on the wall from synchrotron radiation and then go through three different types of processes, producing secondary electrons known as either true secondaries, elastically reflected electrons, or rediffused electrons. When electrons col-

lide with the vacuum chamber wall, a certain fraction scatters back elastically (the elastic secondaries), another fraction interact with atoms inside the wall material and are scattered back out (the rediffused secondaries), and the remainder of the electrons interact through complex processes with the chamber wall (the true secondary electrons) [5]. The following figure taken from [5] displays how each of the three secondary components contribute for an incident electron beam with 300 eV of energy. Fig. 1 shows that the the low energy secondary electrons are dominated by true secondaries, and higher energies are prevalently rediffused and elastic.

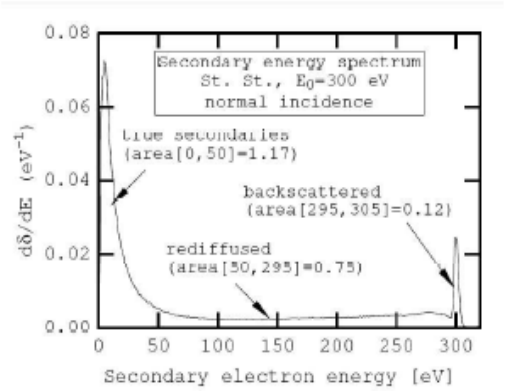

FIG. 1: This plot taken from Furman and Pivi's paper graphs the measured secondary electron energy spectrum for a stainless steel sample to show the contribution from each secondary energy component. The true secondary yield for this plot was 1.17, the rediffused yield was 0.75 and the elastic yield was 0.12. It is worth noting that the true secondary energies used in [5] go up to 50 eV, which is much higher than seen in the ECLOUD code.

II. MEASUREMENTS

The Cornell Electron Storage Ring Test Accelerator (CesrTA) group focuses on electron cloud build up studies and experimenting with mitigation techniques in custom vacuum chambers. This paper's study focuses particularly on two 1.1 m sections located symmetrically in the east and west regions of the storage ring. For summer 2011, the vacuum chamber in the west has been coated in titanium nitride which corresponds to the data used in this study, while the east is coated in a carbon material. Cloud development in the custom chambers is studied using retarding field analyzers (RFA) and two pairs of shielded pickups which are shielded against the signal directly induced by the beam. The RFA is an integrating device that transmits electrons with energy greater than the retarding grid voltage. The shielded pickups were installed in 2010 and have successfully given a wide range of time-resolved measurements of signals from cloud electrons. Each pickup port has an 18 mm diameter pattern of 169 0.76 mm-diameter holes set up in concentric circles, and the center of the pickup buttons are -14, 0, and 14 mm from the horizontal center of the chamber [4]. Fig. 2 depicts one of the custom vacuum chambers and two pairs of shielded buttons arranged parallel and perpendicular to the beam direction. Fig. 3 is a cross section of this vacuum chamber, displaying how the shielded pickup buttons cover the beam pipe

ceiling and the attached electrons and instruments that take measurements. Fig. 4 is a zoomed-in image of one these shielded pickups with a rough sketch of electron collection. Fig. 4 also displays a zoomed-in image of the hole pattern in the vacuum chamber wall that blocks out the beam signal.

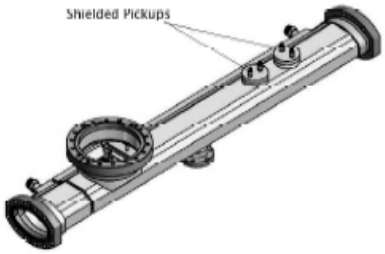

FIG. 2: Custom vacuum chamber with shielded pickups and RFA port [4].

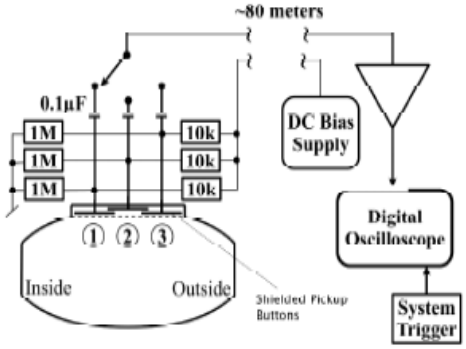

FIG. 3: Vacuum chamber cross section showing three of four shielded pickups and the attached electronics.

Our group concentrates on three types of data sets to study different aspects of the cloud. In current scans, higher beam currents giver larger momentum kicks to cloud electrons. A positron beam pulls floor electrons up into the shielded pickups, while an electron beam pushes electrons above the beam line. Since the button signal arrival time depends on both beam kick strength and intrinsic photoelectron energy, different beam kick strengths are used to distinguish the two contributions to the cloud kinetic energy. In solenoid scans, varying the solenoidal field through the beam pipe and observing which buttons receive a signal is used to determine the energy of electrons, because higher energy electrons produced on the wall will reach a shielded pickup that is farther away from the original production point on the beam pipe wall. Witness bunch scans use one leading bunch, and then one witness bunch at various delay times to study cloud decay over a period of time. The decay time of the cloud was found to be on the order of 100 ns, but it varied with the elastic yield value.

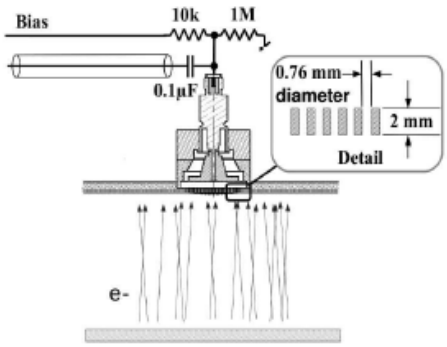

FIG. 4: A close-up of one of the shielded pick-up buttons.

The collecting electrode in the shielded pickup attracts and removes electrons from the cloud. It has been calculated that the total number of electrons that are trapped in the shielded pickup button is negligible compared to the total number of cloud electrons in a vacuum chamber region. Thus the shielded pickups are not causing the cloud to be reduced significantly enough to affect the measurements being taken.

This study focused on electron and positron beams of 2.1 and 5.3 GeV beam energy, a bunch spacing of 14 ns, and a bias voltage of +50 V to prevent contributions to the signal from low energy secondaries escaping the shielded pickup, thus allowing the detector to be sensitive to these low kinetic energy cloud electrons [4]. The data used to compare to the simulation were from the June 2011 runs which I was personally able to take in the control room with James Crittenden and John Sikora on June 11 and 18, 2011. The data was comprised of witness bunch scans, two bunch current scans of 1, 2, 3, 5, 8 and 10 mA per bunch, and one bunch solenoid scans from -40 to 40 G at 1, 2, 4, and 8 mA per bunch. A 1 mA bunch current is equivalent to a bunch population of 1.6E10 electrons. I ran the solenoid simulation for both positron and electron bunches, and the electron beam simulation for current and witness bunch scans, but these were not finished being investigated by the end of my work period and thus are not included in this paper.

III. THE ECLOUD CODE

The program ECLOUD was used in this study to simulate electron cloud build up over the course of a bunch train, and can be set to either positron or electron bunches. As an overview, ECLOUD generates photoelectrons, performs the time sliced kinematics of these electrons, and then creates a detailed model of the secondary electron distribution for the wall.

ECLOUD was written in 1997 and differed from the previously used POSINST code in some details, such as not conserving macroparticle charge. ECLOUD's initial successes include predicting the electron cloud buildup that would be measured at the LHC storage rings and at PEP-II and KEKB. The cloud in these facilities caused tune shift in the leading bunches of particle trains, emittance growth, bunch instabilities, a reduction of specific luminosity, and degradation of various beam diagnostic signals [2]. ECLOUD was initially

created to study the wake field due to the electron cloud, but has the ability to model several important physical processes and effects, including the transverse electron distribution, calculating the total number of electrons and the electron density in the vicinity of the beam as a function of time, the energy spectrum of electrons colliding with the wall and their azimuthal distribution [6]. Other useful options include the ability to add a solenoidal field of different strengths, changing bunch current and delay between bunches, allowing for gas ionization, parameters such as the true, elastic and rediffused secondary yields, separate photoelectron energy distributions for reflected and direct photons, and independent quantum efficiencies for photons produced by direct and reflected photons if the output from the new SYNRAD3D program is used. SYNRAD3D is a program that does photon tracking independent of ECLOUD, then outputs results to be used by ECLOUD. SYNRAD3D determines where the primary photoelectrons are generated. It is important to note that the vacuum chamber shape used by ECLOUD and SYNRAD3D is an ellipse, which is an approximation to the shape of the Cornell beam pipe. The true shape can be seen in Fig. 3. Studies are currently underway to correct this.

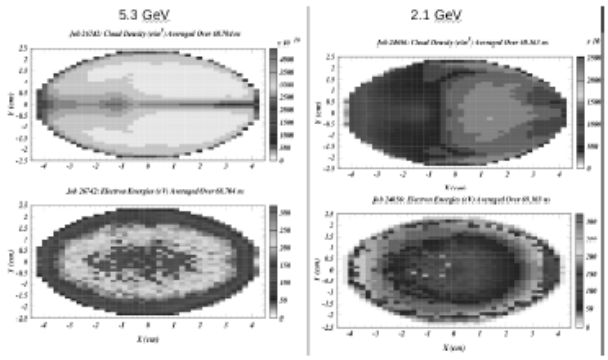

FIG. 5: Cross sectional cloud electron density and energy are compared for 5.3 GeV (left column) and 2.1 GeV (right column). These plots were generated from the simulation in Fig 10. Note that this cross section from the ECLOUD simulation is an ellipse, so it is only an approximation to the real shape that can be seen in Fig. 3, which has not yet been put into the code.

In ECLOUD the cloud electrons are represented by macroparticles, and a typical simulation used on the order of a million macroparticles produced per bunch. More macroparticles means smaller error bars, but a larger run time. For studies presented here, one million macroparticles corresponded to approximately two hours of run time. In POSINST, a random integer n between 0 and a given upper bound is generated with a probability distribution, where n is the number of secondaries that is actually generated. An energy distribution for the new secondaries is then generated under the constraint that the sum of the energies from each electron is less than the initial incident energy. n independent polar angles are chosen with a probability density, and n independent azimuthal angles with a probability density are then generated to be the emission angles of the secondary electrons. ECLOUD differs by generating only one macroparticle per electron impinging on the wall, where the macroparticle has a weighted charge which is the sum of all three yield components. The ratio of one yield component value to the total yield value gives the probability that the kinematics associated with that particular yield type will be used, and only one type of

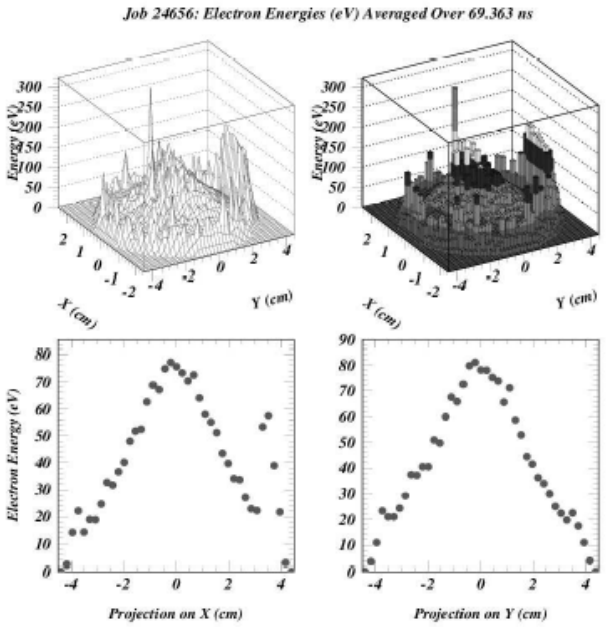

FIG. 6: Contour plot of cloud electron energy inside the beam pipe cross section and x,y projections.

kinematics is used per macroparticle. This means that the kinematics are only correct when averaged over a large sample, as individual macroparticles may be too heavily dependent on one specific component's kinematics too agree with the physical process actually occurring. POSINST generates the correct kinematics for each wall collision, since a distribution of secondaries is produced when an electron collides with the wall [7].

In ECLOUD, when a bunch passes, new photoelectrons are generated and electrons still existing from past bunch passages receive a momentum kick from the beam field, which causes macroparticles to be pushed into one of four shielded pickups on the beamline ceiling and gives a signal proportional to the number of electrons collected. An electron that impinges on the beam pipe wall is replaced by a secondary electron, with a new macroparticle charge that depends on the secondary emission yield at the energy of the incoming electron [6].

After the passage of a bunch, the electron cloud should be dominated by low energy electrons interacting with the wall primarily through the elastic process. High energy electrons of more than 100 eV predominantly go through the true secondary yield process so that the produced secondaries have only on the order of 1 eV. These high energy electrons are present as a result of synchrotron radiation, beam kicks, or the rediffused secondaries [4].

The ECLOUD code also takes into account the physical dimensions of the Cornell synchrotron and beam. The beamline circumference is 768 m. The vertical beam size for 2.1 GeV was 0.044 mm and the horizontal beam size was 0.81 mm. The vertical beam size for 5.3 GeV was 0.29 mm and the horizontal beam size was 1.1 mm. The horizontal aperture limitation was 0.045 m and the vertical aperture limitation was 0.025 m. The RMS bunch

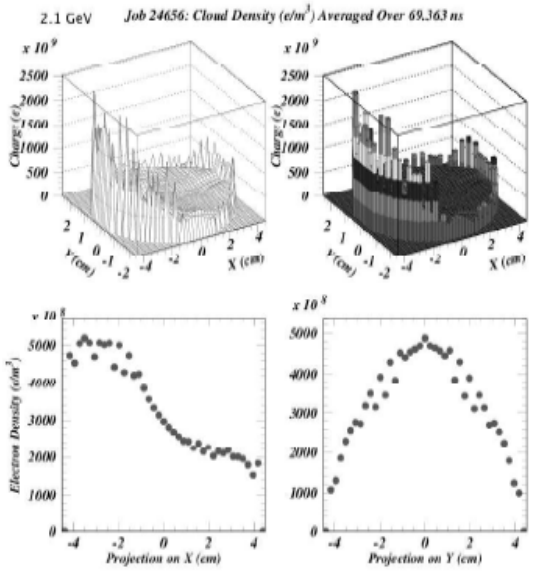

FIG. 7: Contour plot of cloud electron density inside the beam pipe cross section and x,y projections.

length was 1.87 cm.

Fig. 5-7 are examples of the sophisticated diagnostic plots that ECLOUD can produce by tracking the kinematics of the macroparticles. Fig. 5 is an image of the cross section of the vacuum chamber and plots the energy distribution and density of cloud electrons across the beam pipe cross section at 2.1 and 5.3 GeV. Notice that the cloud is densest at the right side of the beam pipe where the synchrotron radiation impinges at the highest intensity, and that the highest energy electrons are found close to the beam in the center of the pipe because of Coulomb attraction. Fig. 6 and Fig. 7 are contour plots and x-y projections of Fig. 5.

IV. RESULTS

A. Secondary Energy Distributions and SEMAX

The original ECLOUD default for secondary energy distribution was chosen by Noel Hilleret from Phil. J. Res. 50 (1996), 375. The function, as seen in the left plot in Fig. 8, was:

$$f(E_{sec}) = \exp(\frac{-\ln(\frac{E_{sec}}{SEMAX})^2}{2})$$

A modification suggested by Miguel Furman that is plotted on the right in Fig. 8 is :

$$f(E_{sec}) = E_{sec}\exp(\frac{-E_{sec}}{SEMAX})$$

where E_{sec} is the energy of the secondary electrons and SEMAX is a constant. Comparing the witness bunch plot in Fig. 9 to the ones in Fig. 10 displays the effects that the default secondary energy distribution had on the witness bunch simulation compared to the more recently used function from Furman. As plotted in Fig. 9, the default function gave witness bunch peaks that had too early of a rising edge, as well as an incorrectly large signal following the leading bunch. The optimized results that used Furman's function are the plots in Fig. 10.

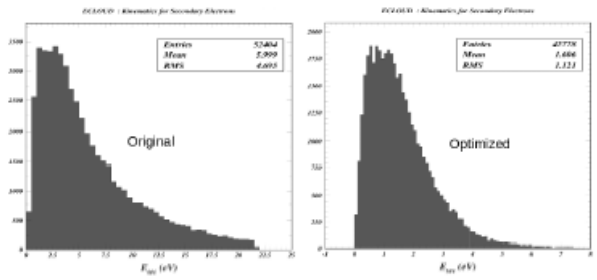

FIG. 8: The original energy distribution is displayed on the left, while Miguel Furman's optimized function that improved simulation agreement with data is displayed on the right. The original distribution has many more high energy electrons which causes early and peaks and a larger signal after the leading bunch than is seen in the data.

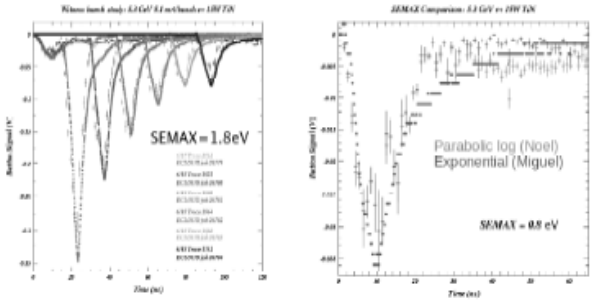

FIG. 9: The left plot shows the best fit that the original secondary distribution by Noel Hilleret with the default SEMAX value of 1.8 eV could give up to the beginning of the summer. Note that this gives leading edges that are too early on the leading edge of the witness peaks. The plot on the right zooms in on the leading bunch and demonstrates that Noel Hilleret's distribution causes too high of a signal after the leading bunch which is apparent at a SEMAX value of 0.8 eV and becomes worse as SEMAX is increased. This incorrectly large signal is not seen in the new distribution.

The late peak after the leading bunch for an SEMAX value above 0.8 eV is seen also in 2.1 GeV, though it is not as obvious for 5 mA bunches because of the lower beam energy. However, if 8 or 10 mA is used, the late signal size compared to the leading bunch signal is closer to the relationship seen in 5.3 GeV. A value of 0.7 eV was found to be a better fit to data in 8mA as 0.8 eV caused too low of a leading bunch signal in the simulation for the 8

mA current value. 10 mA was even lower and the optimum SEMAX value was not tested at this current. 10 mA had other fitting problems in the current scans as well that will not be discussed in this paper.

B. Photoelectron Energy for Direct and Reflected Photons

The low energy component of the photoelectron energy distribution for direct and reflected photons is modeled by a Gaussian, while the middle and high energy components are defined by the following power law:

$$f(E_p) \sim \frac{{E_p}^{p_1}}{(1+\frac{E_p}{E_0})^{p_2}}$$

where E_p is the energy of the primary photoelectrons and E_0, p_1, and p_2 are parameters to be determined. The low, medium and high energy distributions are then weighted and combined to create the simulation peak shapes to compare to the data. The reflected photoelectron distribution primarily affected the leading bunch in the witness scans. The simulation was matched to the leading bunch shape by turning each component's weight to 1 while the other two were set to zero, and then observing which component's contribution needed to be weighted the most to obtain the proper peak shape for the leading bunch.

For 5.3 GeV, both reflected and direct had p_1 set to 3.4 and p_2 to 5.2 in both the reflected and direct distributions' middle component. In the high energy component for 5.3 GeV, p_1 was set to 4.0 in both reflected and direct, but p_2 had a value of 7.2 in direct and 5.6 in reflected. At 2.1 GeV, in the middle energy component, p_1 was set to 3.4 in both reflected and direct, but p_2 had a value of 5.0 in direct and 5.6 in reflected. Both reflected and direct had p_1 set to 4.0 and p_2 to 7.2 in both the reflected and direct distributions' high component.

C. 2.1 and 5.3 GeV Witness Bunch Scan Simulations

The main end results of this summer were successfully matching simulations to data with the 2.1 GeV and 5.3 GeV 5 mA per bunch witness scans, where the final results are shown in Fig. 8, and finding upper and lower bounds for the SEMAX parameter at both 2.1 and 5.3 GeV. Fig. 11-13 plots the process of tuning the SEMAX values.

For 2.1 GeV at 5 mA per bunch, the optimum direct and reflected quantum efficiency value was found to be 0.004 and 0.032 respectively. The optimum SEMAX value was determined to be 0.8 eV. The best values for the weights of the low, medium, and high energy components of the photoelectrons produced by direct photons were found to be 0.5, 0.5, and 0 respectively, while the values of these components for photoelectrons created by reflected photons was found to be 0.65, 0.35 and 0. The true secondary yield was determined to be 0.99, the elastic 0.01, and the rediffused 0. These values were obtained by comparing many simulations with various parameter values to the data sets until the optimum values were found.

Comparing this to the 5.3 GeV 5 mA scans, the the optimum direct and reflected quantum efficiency value was found to be 0.03 and 0.24 respectively. The optimum SEMAX value was determined to be 0.8 eV. The best values for the weights of the low, medium, and high energy components of the photoelectrons produced by direct photons was found to be 1,0 and 0 respectively, while the values of these components for photoelectrons created by reflected

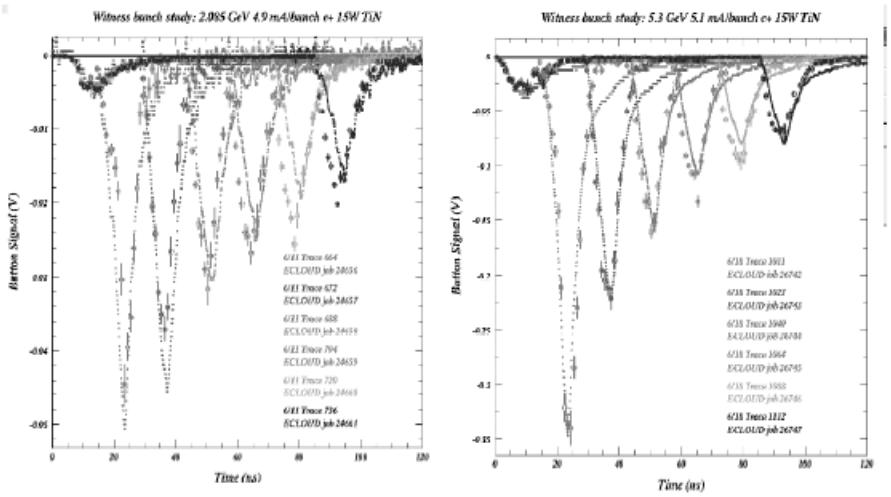

FIG. 10: Successful fitting of 5.3 and 2.1 GeV June 2011 data to simulation of witness bunches.

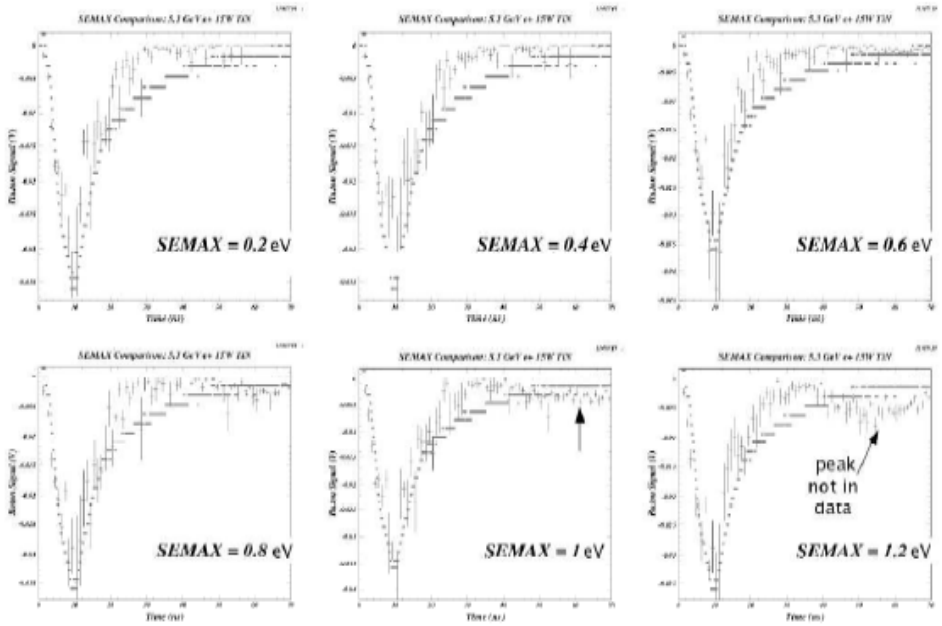

FIG. 11: As SEMAX is increased above 0.8 eV, a late simulation peak appears that is not present at the data.

For both beam energies the angle cut for emitted photons was 35 °, the wake field option

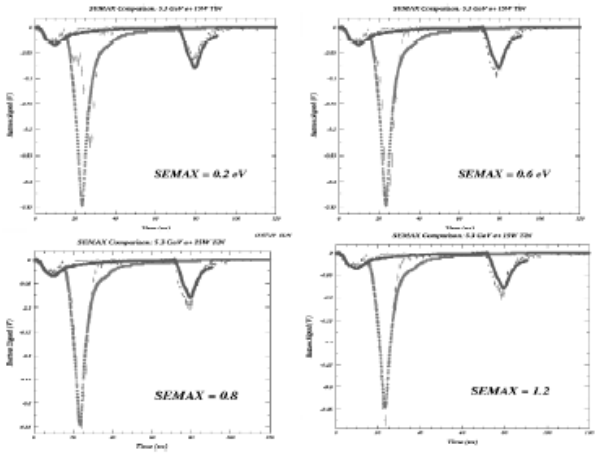

FIG. 12: For SEMAX values less than 0.8 eV, the 14-ns witness bunch signal becomes too small and late.

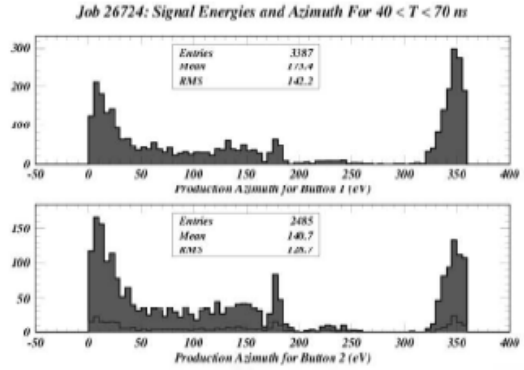

FIG. 13: Photoelectrons from the top of the beam pipe and from direct photons produce secondaries that cause the late signals seen at higher SEMAX values.

was turned off and the energy at which maximum secondary emission yield occurs was 300 eV. The number of times the space charge field is calculated during and between bunch passages is eleven. There were 100 intermediate steps between bunch passage and 400 intermediate steps per inter bunch drift.

Also in both the *splat* function was turned on to set an energy cutoff for high energy electrons that can be accepted by the shielded pickup signal simulation. The splat function represents the physical effect where the shielded pickup signal is a function of incoming energies. At higher energies, the pickup becomes less efficient. The final form of this setting was obtained from tuning modeled pulse shapes.

V. CONCLUSIONS

Both 5.3 GeV and 2.1 GeV have made great progress in describing the shielded pickup witness bunch data. The optimum SEMAX value for agreement between simulation and data was determined to be 0.8 eV at 5 mA per bunch at both beam energies because above this value a late, broad peak not seen in the data appears and below this value the 14-ns witness bunch signal shape does not match the data. The sensitivity to this parameter is 0.2 eV, which is a surprisingly large dependence. Miguel's exponential distribution gives a better match than the Phil. J .Res. parabolic log function.

A. Future Work

Future work will require integrating the real vacuum chamber pipe shape into the simulations and retuning the parameters if needed to agree with the data once this is done. The simulation also needs to be corrected to better agree with data from solenoid and electron scans.

VI. ACKNOWLEDGMENTS

I would like to express gratitude to my mentor Dr. James Crittenden for proposing this REU project and offering advice in tackling the many problems this research presented. Also, thanks to Dr. John Sikora for advice on presentations and simulation improvements. Thanks also to those whose efforts made the REU program possible including Lora Hine, Monica Wesley, Dr. Ivan Bazarov and others.

VII. BIBLIOGRAPHY

[1] K.C. Harkay, R.A. Rosenberg. *Properties of the electron cloud in a high-energy positron and electron storage ring.* Phys. Rev. ST Accel. Beams 6, 034402, 2003.
[2] K. Ohmi, F. Zimmerman, G. Rumolo. *Electron Cloud Build Up in Machines with Short Bunches.* ICFA Newsletter no. 32, May/June 2004.
[3] F. Zimmermann, E.Benedetto. *Electron-Cloud Effects in the LHC.* ICFA Newsletter no. 32, May/June 2004.
[4] S. Calatroni, J.A. Crittenden, Y. Li, X. Liu, N. Omcikus, M.A. Palmer, G. Rumolo, J.P. Sikora. *Electron Cloud Modeling Results for Time-Resolved Shielded Pickup Measurements at CesrTA*. Proceedings of ECLOUD 2010: 49th ICFA Advanced Beam Dynamics Workshop on Electron Cloud Physics, Ithaca NY.
[5] M. A. Furman, M.T.F. Pivi. *Probabilistic model for the simulation of secondary electron emission.* Phys. Rev. ST Accel. Beams 5, 124404, 2002.
[6] G. Rumolo, F. Zimmerman. *Electron-Cloud Simulations.* http://conference.kek.jp/two-stream, 11-14, September 2001 KEK.
[7] Private conversation with James Crittenden. July 29, 2011.

CERN Summer Student Report

August 8, 2012

ISF Hadronic Interaction Studies in the ATLAS Inner Detector

Ryan Badman[a] and Elmar Ritsch[b]

[a]*Syracuse University*
[b]*ATLAS Experiment*

Abstract

This paper summarizes a summer student project done the summer of 2012 for Elmar Ritsch. Hadronic interactions were studied in the inner detector for both Geant4 and Fatras using a Geant4 hadronic interaction processor. The number of child particles and their types were looked at for each simulator, and first attempts at parametrizing the hadronic interactions inside the inner pixel layers and SCT for the ATLAS detector were made.

1 Introduction

By 2015, the ATLAS experiment will have surpassed the limits of the amount of data it can handle in a reasonable amount of time. Using Monte Carlo simulations to model particle interactions inside the detector is an increasingly complex and computationally intense task, but is vital for data analysis. This is in large part because the very small cross-sections for new physics signatures with respect to background processes need a large quantity of events for the simulation. The greatest portion of computing time is spent on the active and passive interactions with the detector material, and as ATLAS is the biggest particle detector in volume ever created and is packed with tiny complex circuits, doing this modeling in the very detailed full simulation Geant4 is not always feasible. Fatras, a fast track simulation engine of the ATLAS inner detector and muon system, is a way around this by parametrizing the calorimeter response. So far, Fatras' agreement with Geant4 has been extremely promising and reduces the computing time by two orders of magnitude [1].

2 Geant4

Geant4 is software package that very accurately simulates particle interactions with matter. It contains detailed information of the geometry of the system, the materials particles will interact with, the particle properties, tracking through materials and electromagnetic fields, the physics processes governing the particle interactions, detector response properties, event data generation and storage, and user-friendly analysis at different levels of detail for simulation data. Geant4 is basically a package that incorporates a large portion of the complete accumulated knowledge we have about particle interactions [2].

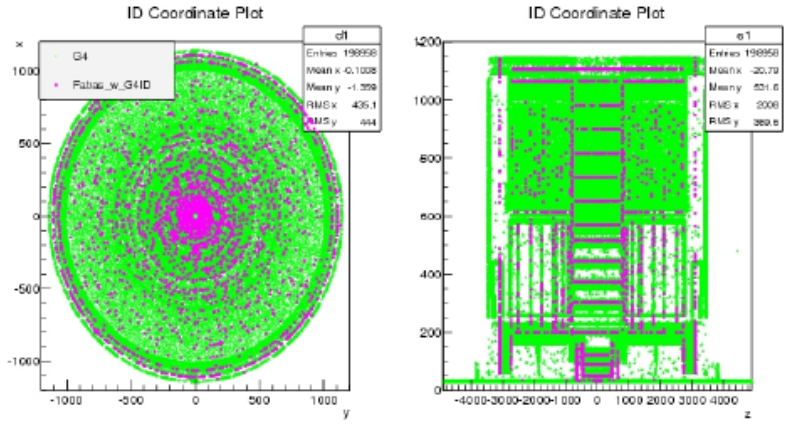

Figure 1: These are X-Y (left) and R-Z (right) coordinate plots that show the Geant4 interactions throughout the detector volume (green) versus Fatras interactions on projected surfaces (purple).

3 ISF

The Integrated Simulation Framework (ISF) is a framework that allows different simulation engines, such as Fatras and Geant4, to be selected to carry out the particle physics in the detector. In the center is the SimKernal, an Athena algorithm which has a few simulation services, one particle broker service for particle routing and one truth service to record information about their interactions. The SimKernal controls an ISF particle loop which retrieves one particle to be simulated from the ParticleBroker and sends it to an assigned SimulationService. First the geometrical flag is checked in the particle passport. Then the particle is forwarded to a sub-detector simulation service. The stack service and truth record services are also passed for consistency checks and to make it so there is only one configuration setup for all components.

The ISimulationSvc builds the interface for both sub-detector services and flavor simulation services. The flavor simulation services receive the stack particle, and the stack and truth record service, and perform a simulation until either the particle decays within the sub detector volume and the truth incident information is stored with the decay particles sent to the stack; the particle leaves the sub detector volume and is returned to the stack simulation, or the particle is killed due to cuts such as momentum or energy thresholds.

The ISF is projected to be ready by 2013-2014 and will be used for all simulations and larger scale Monte Carlo productions starting in 2015 due to the much higher integrated luminosity that the LHC will be using. It will also have applications in parallel computing techniques. By allowing users to select between the more accurate Geant4 full simulation and faster simulations like Fatras FastSim, users can more easily optimize between accuracy and precision and faster run time for process details that are not as important depending on the analysis goals [3]. Figure 2 displays an image of how the ISF process works.

4 ATLAS

The ATLAS detector's primary mission is to discover new physics, particularly SUSY or the nature of the Higgs Boson. The inner detector and the muon system are tracking systems to measure the momenta of particles coming off the collision, and the calorimeters record their energies. The inner detector, which this study focuses on, has three subsystems. The pixel detector is immediately around the beam line and determines the origin of the hard scattering processes and the secondary vertices' positions from unstable particles with a longer lifetime. The two other inner detector components are the Semiconductor Tracker and the Transition Radiation Tracker, and were installed to the provide more precision hits to reconstruct charged particle tracks [1]. This study focused on only hadronic interactions inside the inner detector.

5 Hadronic Interactions

Hadronic showers are ones in which the shower development is heavily influenced by the strong interactions between shower particles and the atoms of the absorbing material. Hadronic interactions have turned out to be much more difficult to simulate than electromagnetic showers and there is a much larger variety of interaction kinds that can occur.

One main difference between electromagnetic showers and hadronic showers is that in hadronic showers, a certain fraction of the dissipated energy is inherently unable to be detected. When a high energy hadron traverses a medium, many of the processes seen in electromagnetic showers will occur, such as atoms of the medium being ionized in a continuous stream of events similar to the behavior seen with muons. The difference starts when the hadron meets an atomic nucleus and begins interacting strongly. This can results in a plethora of different outcomes: for example many new hadrons could be

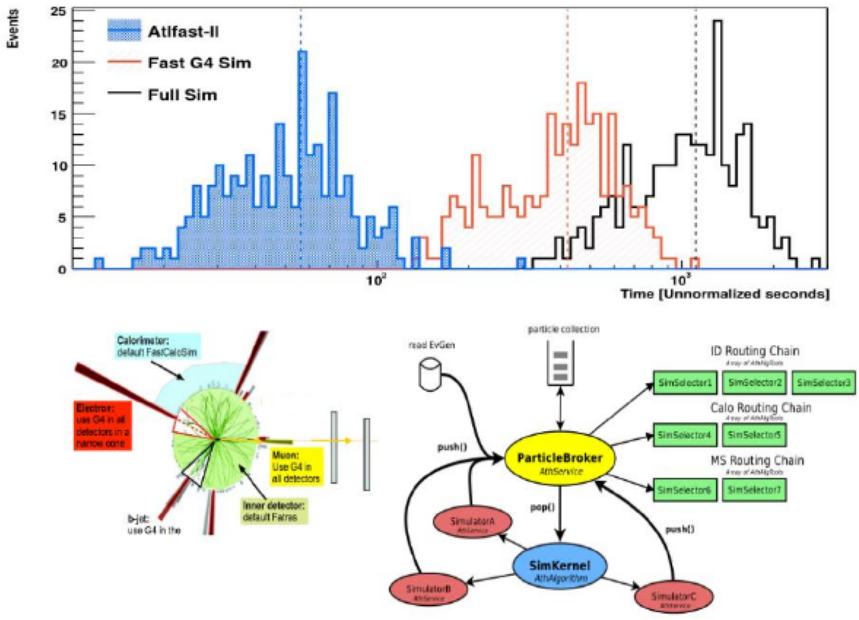

Figure 2: The top plot compares simulation time for Geant4, Fatras, and the Fatras/Geant4 hybrid. The bottom shows the map of the ISF process [3].

produced, or the material nucleus could be greatly altered or go into an excited state. Neutrons can only do these nuclear interactions because of their absence of charge.

The missing energy comes in during spallation, the most likely hadronic interaction process between the shower particle and nucleus. Spallation is a two step process with a fast intranuclear cascade being the first and a slower evaporation stage being the second. In spallation, many nucleons may be released from nuclei. The nuclear binding energy required to eject these nucleons is lost from the calorimeter. However, this can be accounted for by using the correlation between invisible energy lost when nucleons are kicked out of the nucleus and the kinetic energy these nucleons have as they come out. [4].

6 Results

The first part of this study was validating Fatras with the Geant4 Hadronic Interaction processor against pure Geant4 in the ATLAS inner detector. ttbar collisions were used. The plots in Figure 1 show how the Geant4 sample that was used for validating against successfully used complex interactions throughout the

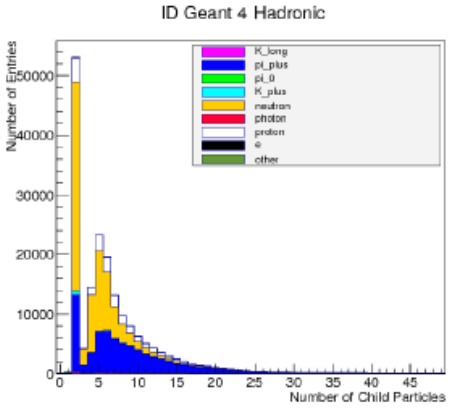

Figure 3: Plot of number of child particles per parent for different particle types for Geant4,ttbar. Notice the peak at two particles not seen in Fatras. This is due to nuclei elastic interactions that can be neglected due to the short travel distance of the nuclei.

whole detector volume, but Fatras projected these volume interactions into simpler surface interactions on layers throughout the detector.

An initial peak at two child particles from protons and neutrons were originally seen in Geant4 (Figure 3), but not Fatras (Figure 4), but this peak was eliminated when it was found that these were due to elastic collisions against nuclei, and the nuclei coming off traveled only very small distances in the detector and could be neglected. After this change and some other debugging in Fatras, the final agreement between Fatras and Geant4 can be seen in Figure 5.

The second main part was making initial steps to parametrize the hadronic interactions inside the pixel layers in the inner detector. This was done using a truth strategy by Elmar Ritsch that set a vertex at each step of the particle tracking between pixel layers so that an analysis code could be used to find the number of hadronic interactions that occur inside each pixel layer and the number of resulting outgoing particles. For this study single pions were used because they have much smaller showers and would take less time with the new, more output dense truth strategy.

It was found that for, for 10000 pion events, for the first pixel layer, twenty-three particles came in and hadronically interacted producing ninety-seven child particles that left the layer. In layer 2 five particles came in for a hadronic interaction and eight left, and for the third layer seven particles came in and eight left. The probability that a high energy hadron traverses a distance z in a medium with nuclear interaction length λ without causing a nuclear interaction is

$$P = \exp[-\frac{z}{\lambda}] \tag{1}$$

The ratio of z to λ was 0.015 for the inner detector region under study. This means that for 10,000 events, 140 interactions should have been seen. Our number was low at only twenty-three.

7 Conclusion

The validation between Geant4 and Fatras using the Geant4 hadronic processor is very promising. The truth strategy and analysis code was successfully able to simplify the Geant4 volume interactions inside

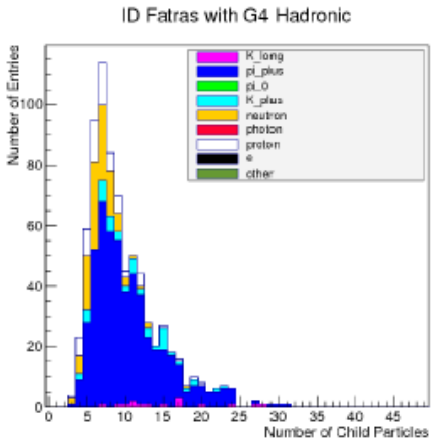

Figure 4: Plot of number of child particles per parent for different particle types for Fatras,ttbar.

the pixel layers by seeing on average how many particles come in and hadronically interact, and then how many leave as a result. Further study may allow these pixel layer, and also SCT, processes to be completely parametrized.

The fact that the number of hadronic interactions is lower than theory predicts could be corrected by forcing hadronic interactions inside the pixel layer according to the probability that they should occur. This could become a permanent and important feature in the ISF framework, but more studies need to be done.

I would like to acknowledge my advisor Elmar Ritsch for his prompt email replies and easy accessibility which made this summer's project very fruitful and greatly facilitated my learning process. I would also like to thank Wolfgang Lukas and Andreas Salzburger for their help and willingness to answer questions whenever I needed. Finally I would like to thank the NSF and the University of Michigan for making this program possible and being so supportive of the US summer students it sends to CERN.

References

[1] Mechnich, Jorg (on behalf of ATLAS), *FATRAS-the ATLAS Fast Track Simulation project*. J. Phys.: Conf., 331 (2011) 032046. doi:10.1088/1742-6596/331/3/032046

[2] Geant4 Collaboration, *Geant4 User Documentation: Introduction to Geant4*. Available on http://geant4.web.cern.ch/geant4/support/userdocuments.shtml", Last Updated 2011.

[3] Lukas, Wolfgang, *Fast simulation for ATLAS: Atlfast-II and ISF*. CHEP 2012 Poster Session, 21-25 May 2012, New York (USA).

[4] Wigmans, Richard, *Calorimetry: Energy Measurement in Particle Physics*. Oxford University Press Inc, New York, 2000.

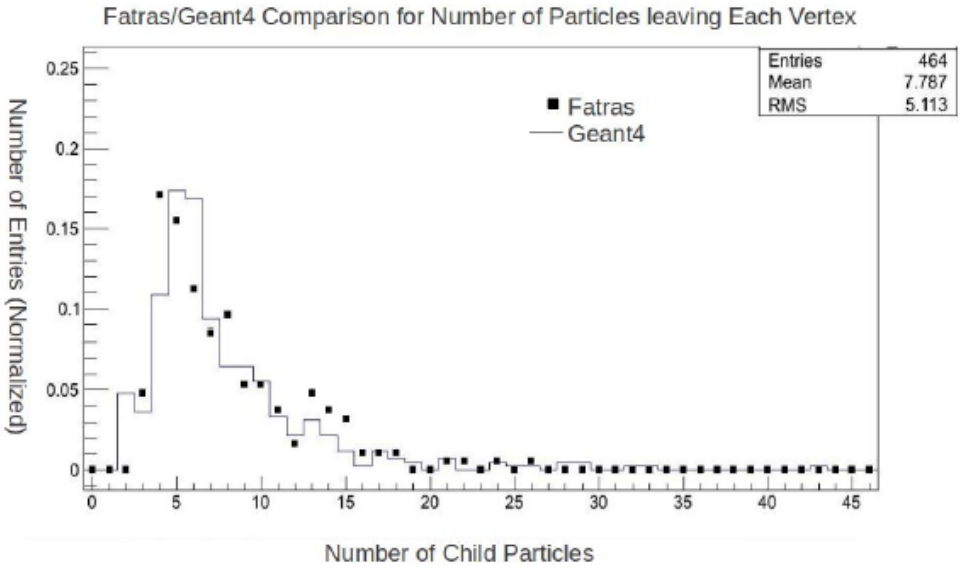

Figure 5: Current agreement between Fatras and Geant4 for number of out particles per vertex.

I. INTRODUCTORY NOTES ON ACCELERATOR PHYSICS

Particle accelerators have provided many benefits to both intrinsically interesting fundamental science and pragmatic applications. In nuclear and particle physics, there have been many famous particle accelerators that have been integral in forwarding the understanding of the processes that govern the universe at the smallest size scale. First and foremost is the Large Hadron Collider (LHC) in Geneva, Switzerland, where a Higgs boson discovery was announced this past summer after years of data collection and analysis. This boson, a particle with integer spin, is thought to be a manifestation of the Higgs field which is proposed to be the source for mass in the universe.

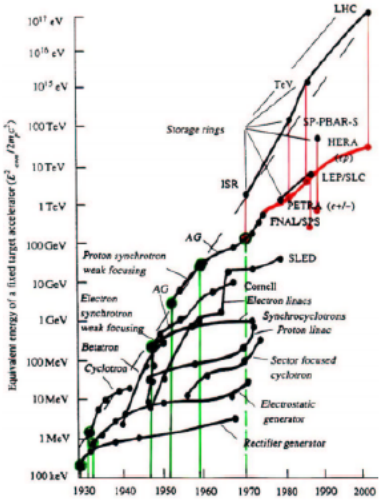

FIG. 1. The progress in particle accelerator energy over the past few decades is commonly shown in the Livingston chart, where the slope of the dotted line gives a rate of increase of an order of magnetic of energy roughly every seven years due to a history of periodic innovations in accelerator research.

I worked on ATLAS, one of the two experiments at CERN that was responsible for the Higgs' discovery this past summer (the other being CMS) and the second part of my capstone will be a brief summary of this work. Accelerators have also been useful in industry and the biomedical field for ion implantation, lithography, mapping the structure of viruses, breaking down nuclear waste, proton beam cancer treatment and X-ray imaging with high energy synchroton radiation, as is done at the Cornell synchroton where my capstone was primarily completed. The superconducting research vital for modern accelerators to work has have provided many boons for society as well through the development of materials that conduct electricity with zero resistance, such as the rails that allow high speed Maglev trains to run. As of 2011, approximately 120 accelerators are used for particle physics research, 70 electron storage rings and electron linear accelerators are used as light sources and X-ray

studies, 7,000 accelerators are used for medicine and radiotherapy, and 18,000 for industry such as ion implantation and electron cutting and welding.

FIG. 2. The percent of particle accelerators used in different fields.

Particle accelerators have improved drastically since the 1930s, when high energy was considered to be the MeV scale. The LHC is currently running energies on the order of 10 TeV, with beam intensities of 10^{14} particles per pulse compared to the 10^{9} seen in the 1950s [1]. This outstanding progress is commonly shown in the Livingston chart, as shown if Figure 1, where the slope gives a rate of increase of an order of magnitude of energy roughly every seven years for proton machines (lepton machines have a smaller slope) due to a history of periodic innovations in accelerator research [2]. The general principle is that higher energies provide new discoveries and higher luminosity gives more precise measurements.

The LHC and the Cornell synchrotron differ at the most basic level in that the LHC is a hadron accelerator, which collides protons and antiprotons, and the Cornell synchrotron collides leptons. According to Lee, for high energy hadron accelerators, "high-field superconducting magnets and the stability of high-brightness beams are the important issues. For lepton colliders, high acceleration gradient structures, wakefields, and high power radio frequency sources are important" [1]. These magnets and RF generators are briefly discussed below. Hadrons are heavier and have a multi-quark substructure, so their collisions tend to cause particle processes and decays that are of much greater complexity. Leptons, which are usually electrons and anti-electrons, are over three orders of magnitudes smaller in mass and are thought to be fundamental particles. Thus their collisions have simpler particle final states and are better used for precision measurements.

The first accelerators used electrostatic fields, a common example being the Van De Graaf Accelerator. However in the megavolt range this type of accelerator breaks down. Starting in 1928, accelerators called drift tubes began using radio frequency (RF) generators, in which metal cylinders are lined up with one cylinder being positive charged, the next being negative, the next being positive and so on alternating positive and negative as seen in Figure 3. The limitations of RF are that the particles have to travel in groups called "bunches" and the energy is directly proportional to the frequency of the RF cycles, which turns out to be maxed around 10 MHz so it is not useful for very relativistic particles. The cyclotron invented by E. Lawrence in 1929, was a new innovation that curved the straight line accelerated particle trajectory into a spiral. As a particles speed approaches the speed of light, the $\gamma = \sqrt{1 - v^2/c^2}$ factor causes the energy needed to accelerate to rapidly increase, where energy $E = mc^2$ and c is the speed of light [3].

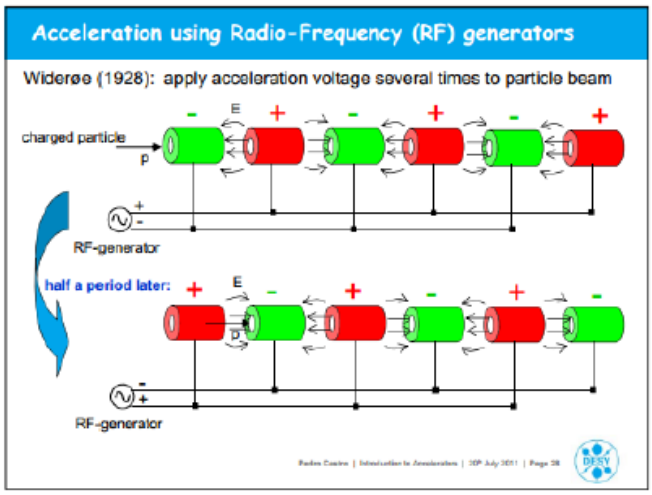

FIG. 3. This figure shows how alternate charged drift tube RF generators are used as accelerators. As a particles speed approaches the speed of light, the γ factor causes the energy needed to accelerate to rapidly increase [3].

In circular accelerators such as cyclotrons and synchrotrons, straight RF cavities are used to accelerate the particles and magnets are used to curve the particle trajectories, each with a force proportional to the field strength. Synchrotrons are accelerators with fixed radii and are more commonly used in research today, while cyclotrons are smaller with a variable radius and are commonly used for proton therapy in the medical field. In large circular accelerators like the LHC, dipole magnets are used to bend the particles, while higher pole magnets (quadrapoles and sextapoles) are used for focusing particles, similar to the way to lenses focus light. These magnets are shown in Figures 4 and 6. The LHC magnet apparatus shown in the top of Figure 6 houses two superconducting electromagnets oriented in opposite directions, shown in the bottom of Figure 6, to generate the magnetic fields for the two proton p beam pipes that run antiparallel to each other. These enormous fields are on the order of 1 Tesla, with a maximum limit of about 5 Tesla. As discussed in the Cornell section of the paper, circular electron beams emit higher amounts of synchrotron radiation so proton beams are easier to get to a higher energy [3]. This is why higher energy lepton accelerators can only be achieved with linear accelerators, such as the proposed International Linear Collider that I contributed to research for at Cornell. As shown in Figure 5, the proposed International Linear Collider (ILC) will use superconducting RF cavities to accelerate positrons and electrons to high energies in the TeV range.

The LHC is the highest energy and highest luminosity hardon collider in the world with the ability to explore the TeV scale of particle physics, and the ILC will be the highest energy lepton collider, the first on the TeV scale, when it is constructed. There are still many problems that need to be solved for each project. For the LHC, there is a need for faster data processing and trigger selection to pick out the important data from the rest as

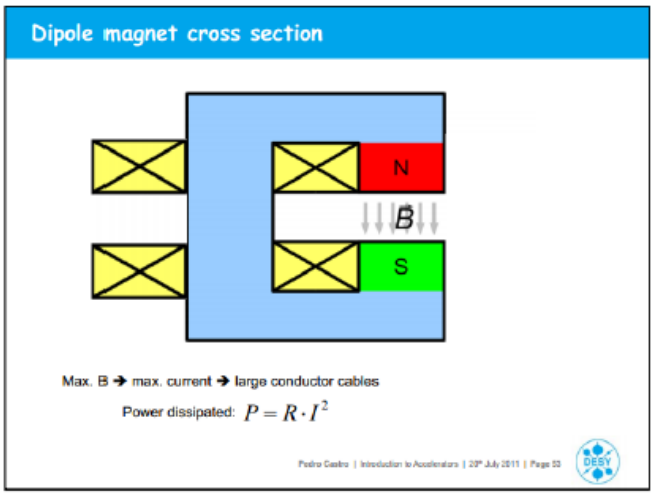

FIG. 4. Cross section of dipole magnet in an accelerator[3].

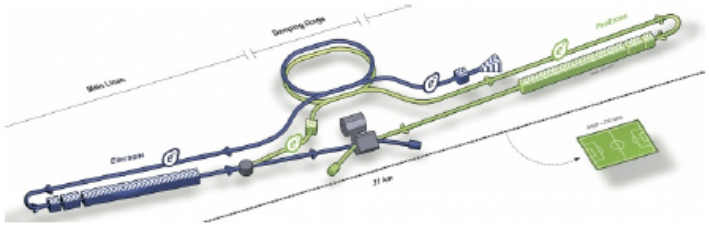

FIG. 5. A diagram of the International Linear Collider which will accelerate and collide leptons. The positron damping rings which my Cornell research focused on are in the circular part of the beam pipe [3].

there is more data collected at a given time than can be stored and processed. Pile-up is also a major issue. In this phenomenon, many decays and collisions occur very close to each other in time or space (or both) and accurate reconstruction is extremely difficult. These problems will require upgrades in both hardware and software, and many projects along these lines will be going on during the shutdown of the LHC from 2013 to 2015, and for a longer shutdown around 2017 or 2018. For the ILC, there are dilemmas such as the electron cloud phenomenon where photoelectrons created as a result of the electron or positron beam radiating the beam chamber walls, which creates a charged cloud that can greatly interfere with the beam. This is the process that I studied at Cornell in 2011 for the positron damping rings and discuss in my first report. Both accelerators have the possibility of discovering new physics and making important precision measurements to test the standard model to degrees of accuracy that have never been achieved before.

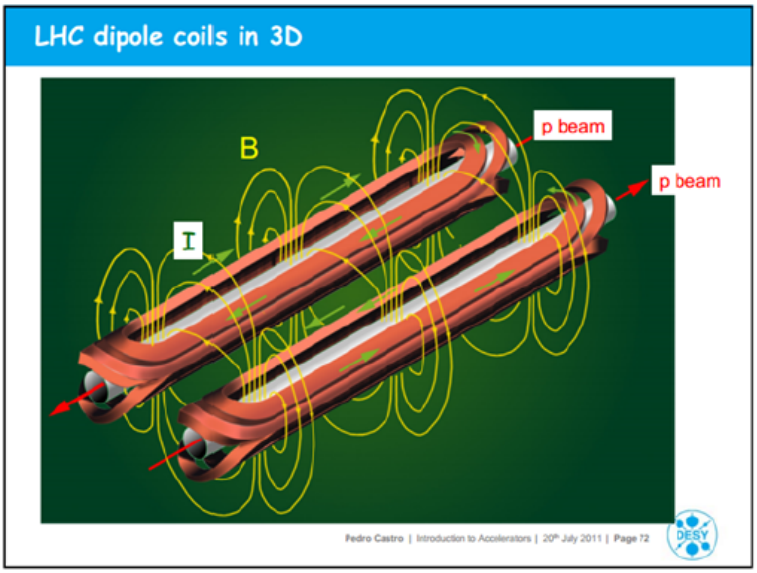

e

FIG. 6. The dipole magnets used at CERN [3].

II. INTRODUCTORY NOTES ON THE ATLAS DETECTOR

The ATLAS experiment, in addition to its recent success with the Higgs boson discovery, see Figure 9 for the characteristic Higgs signal, is also engaged in many other physics searches. The Large Hadron Collider recreates the initial conditions of the universe immediately following the Big Bang, but on a microscopic scale. The universe is made up of roughly five to six times more dark matter than ordinary matter, and the ATLAS detector could discover the particles that dark matter is composed of. String Theory also predicts

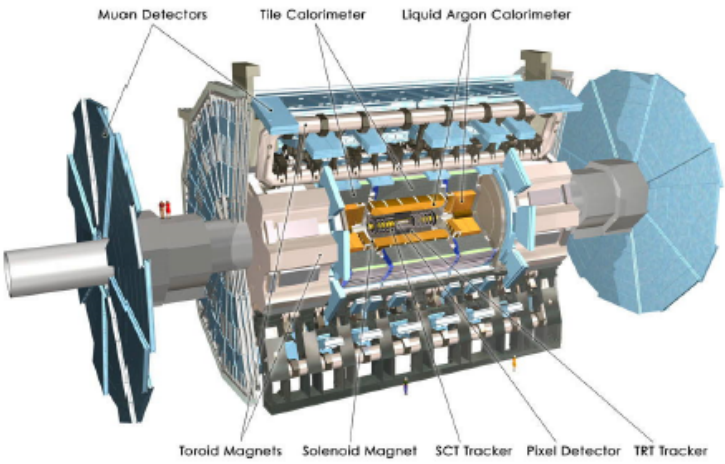

FIG. 7. Schematic of the entire ATLAS detector.

the existence of extra spacial dimensions, and massive partner particles for every currently observed particle in the Standard Model. One of the superparticles could also be the dark matter particle and could be observed in the ATLAS detector. The reason why there is more matter than antimatter in the universe will also be explored, and there is the chance that completely new and unpredicted particles or forces will be observed.

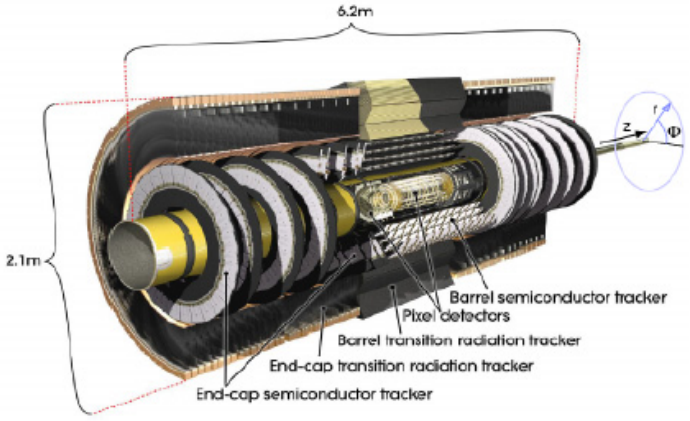

FIG. 8. Schematic of the ATLAS inner detector.

As displayed in Figure 7, the ATLAS detector uses a toroid system that is approximately 20 m in diameter as a muon spectrometer. The electromagnetic calorimeter uses liquid argon to study electromagnetic processes. Hadronic interactions are studied in the "barrel", see Figure 8, which uses an iron and scintillator sampling hadron calorimeter, except at the endcaps which use liquid argon. The tracking system uses layers of silicon strip and pixel detectors in the innermost detector regions, and straw-tube detectors in the outer part of

ATLAS. The ATLAS detector is especially precise in electromagnetic calorimetry, such as for electron and photon identification and measurement, and missing transverse energy in collisions. ATLAS is very efficient in tracking and decay reconstruction at high luminosities.

My summer project at CERN primarily focused on the ATLAS inner detector (ID). The ID's purpose is to reconstruct tracks and vertices from particle collisions with high efficiency. Combined with the calorimeter and muon detector, the ID is very important in studying particles with short lifetimes. The detectors in the ID require a fast processing speed, radiation hardiness, and high resolution. They also have to be as thin and light as possible to prevent problems such as multiple scattering in tracking.

The ATLAS Semiconductor Tracker (SCT) is more than ten times larger in surface area than previous silicon microstip detectors. The barrel (about 2 cm x 80 cm) has four layers of silicon detectors. The ATLAS Transition Radiation Tracker uses 50,000 straw detectors instead of silicon detectors. The straws detectors are narrow tubes full of xenon gas that provide spatial resolution of 170 micrometers.

The Electromagnetic (EM) Calorimeter is a lead liquid-argon detector. It is almost 5 m in diameter and has very high granularity to eliminate the enormous backgrounds that would make observing the Higgs boson very difficult otherwise. The Tile Hadronic Calorimeter is almost 7 m in diameter outside of the EM Calorimeter and uses a combination of plastic scintillator tile plates embedded in iron, and liquid argon detectors. As shown in Figure 7, the calorimeter is in multiple parts to cover particles going in the transverse, forward, and backward directions relative to the beam pipe.

The outermost part of the detector is the Muon Spectrometer. Muons are leptons like electrons, but have a larger mass. Measuring high momentum muons are very important for studying Standard Model and beyond Standard Model decays, such as supersymmetry. The muon spectrometer has three large superconducting air core toroid magnets that deflect muons and measure them with high resolution tracking chambers. Monitored Drift Tubes, which are gas-filled aluminum tubes containing a 50 micrometer central wire, measure the track coordinates of the muons. Other detector components such as the Cathode Strip Chambers are used to provide a finer granularity in measurements [4].

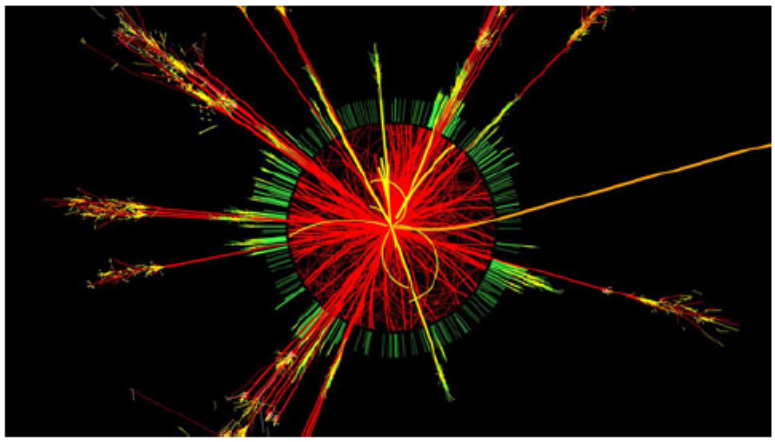

FIG. 9. The Higgs signal.

Quoting the official ATLAS website (http://atlas.ch/), "If all the data from ATLAS would be recorded, this would fill 100,000 CDs per second. This would create a stack of CDs 450 feet high every second, which would reach to the moon and back twice each year. The data rate is also equivalent to 50 billion telephone calls at the same time. ATLAS actually only records a fraction of the data (those that may show signs of new physics) and that rate is equivalent to 27 CDs per minute." My summer project at ATLAS was to help parameterize complex physics processes with simpler mathematical models to make the analysis of the expected mass of data that will start to be collected in 2015 more efficient. This was done through a computer framework called the ATLAS Integrated Simulation Framework. My Cornell REU provided me with with more accelerator physics and hardware studies, and the ATLAS REU concentrated more on particle physics and was computational-based. High energy physics careers require knowledge of each of these components and both studies complimented each other and were integral for my undergraduate training.

III. BIBLIOGRAPHY

[1] Lee, S.Y. *Accelerator Physics (2nd Edition).* World Scientific Publishing Co. Pte. Ltd., 2004. Print.
[2] Teng, L. *Particle Accelerators-Outlook for the Twenty-First Century.* Proceedings of the Second Asian Particle Accelerator Conference, Beijing, China, 2001. 926-933.
[3] Castro, Pedro. *Introduction to Accelerator Physics. DESY, 20th July 2011.*
[4] Efthymiopoulos, I. *Overview of the ATLAS detector at LHC.* ATL-CONF-99-002. June 24, 1999.